

Experimental and Numerical Dynamic Behavior of Bending-Torsion Coupled Box-Beam

*Original*

Experimental and Numerical Dynamic Behavior of Bending-Torsion Coupled Box-Beam / Patuelli, Cesare; Polla, Alessandro; Cestino, Enrico; Frulla, Giacomo. - In: JOURNAL OF VIBRATION ENGINEERING & TECHNOLOGIES. - ISSN 2523-3920. - ELETTRONICO. - (2023). [10.1007/s42417-022-00759-7]

*Availability:*

This version is available at: 11583/2972818 since: 2022-11-04T13:44:50Z

*Publisher:*

Springer

*Published*

DOI:10.1007/s42417-022-00759-7

*Terms of use:*

This article is made available under terms and conditions as specified in the corresponding bibliographic description in the repository

*Publisher copyright*

AIMS postprint/Author's Accepted Manuscript [con art. gia' pubblicato]

This article has been published in a revised form in JOURNAL OF VIBRATION ENGINEERING & TECHNOLOGIES {<http://dx.doi.org/{dc.identifier.doi}>}. This version is free to download for private research and study only. Not for redistribution, re-sale or use in derivative works.

(Article begins on next page)



# Experimental and Numerical Dynamic Behavior of Bending-Torsion Coupled Box-Beam

Cesare Patuelli<sup>1</sup> · Alessandro Polla<sup>1,2</sup> · Enrico Cestino<sup>1</sup> · Giacomo Frulla<sup>1</sup>

Received: 14 June 2022 / Revised: 1 September 2022 / Accepted: 18 October 2022  
© The Author(s) 2022

## Abstract

**Purpose** Structural configurations related to new green aircraft design require high efficiency and low weight. As a consequence, moderate-to-large deformation under operating loads arise and aeroelastic instabilities different with respect to rigid counterpart are possible. Coupled structural configurations can provide the right mean to overcome such a critical situations selecting the right coupling parameters and structural performance. In this work, the dynamic behaviour of stiffened box-beam architecture with selected optimal stiffener orientation to emphasize the bending-torsion coupling characteristics has been investigated.

**Methods** An extensive experimental activity has been performed for a validation and confirmation of the numerical results. Two cantilever beams produced with different technologies and materials have been tested. Modal performance has been determined by means of a laser Doppler vibrometer (LDV), while Finite-Element Method (FEM) numerical simulation based on solid elements and equivalent single layer approach have been applied and compared. Experimental/numerical comparison have been presented pointing out the specific coupling performance of this architecture with respect to natural frequencies and modal shapes.

**Results** The activity demonstrates a good correlation in natural frequencies that remains mostly under 4%. Modal assurance criterion (MAC) has been considered in comparing experimental and numerical modal shapes.

**Conclusion** The proposed innovative configuration demonstrates its capability to be used in aeroelastic critical problem as a mean to reduce their influence in aircraft design. The numerical procedure used for equivalencing the stiffened parts of the box-beam has also been validated in dynamical response confirming the possibility to be used in design phase.

**Keywords** Vibration · Finite element · Modal analysis · Laser Doppler Vibrometer (LDV) · Oblique stiffeners · Equivalent layer

## Introduction

The increasing level of environmental requirements related to CO<sub>2</sub> emissions for civil aviation are pushing forward the structural research activity around the world. The necessity of high efficiency aircraft, such as long-endurance aircraft, leads to high aspect ratio wing structures, which could present large deflections during normal flight situations. These characteristics can increase the occurrence of different aeroelastic instabilities if compared to their rigid counterparts [1–5].

Innovative structural concepts are necessary for the next generation aircraft reducing structural weight and improving structural performance. Static and dynamic aircraft structural and flight performance can be influenced by specific and imposed structural couplings. This innovative

Alessandro Polla, Enrico Cestino and Giacomo Frulla contributed equally to this work.

✉ Cesare Patuelli  
cesare.patuelli@polito.it

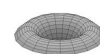
Alessandro Polla  
alessandro.polla@polito.it

Enrico Cestino  
enrico.cestino@polito.it

Giacomo Frulla  
giacomo.frulla@polito.it

<sup>1</sup> Department of Mechanical and Aerospace Engineering (DIMEAS), Politecnico di Torino, Torino, Italy

<sup>2</sup> Department of Aerospace Engineering and Aviation, School of Engineering, RMIT University, Melbourne, Australia



technical solution can be used to cope with such a demanding structural design devoted to reduce/control the aeroelastic instabilities as a primary consequence. Finite element (FE) analysis and numerical optimization can be adopted to improve the structural model. The introduction of innovative solutions such as Variable Angle Tow (VAT) laminates and curvilinear stiffeners significantly enlarged the design space for aeroelastic tailoring [6–12]. Particularly, these innovative solutions introduce a local stiffening effects which may allow structural coupling and postpone critical aeroelastic phenomena typical of High Aspect Ratio (HAR) wing [7, 13, 14].

The increasing complexity of such aeronautical structures requires very accurate numerical simulations during the design phase. Often, those simulations can be very demanding in terms of computational costs. In the early stages of the design process, models which simplify the structure can reduce considerably the time required for the simulation and give reliable results which can be used as a preliminary calculation for the final design. In this research, an equivalent single-layer material model (EQM) developed by Cestino et al. [13, 15] is used to simplify the geometrical local complexity of aluminium stiffened panels. EQM model has been used previously by Danzi [11, 15] to evaluate the buckling loads of a stiffened plate and by Cestino et al. [13] for the analysis of a cantilever beam subjected to static tip load. An extension of the EQM to the dynamic properties of the same box-beam configuration is presented in this work. A complete validation of the potentiality of such structural architecture is also described with reference to previous research activity performed by Pratico et al. [16] specifically related

to stiffened plate. This work paves the way for future studies on the potential for dynamic tailoring of wing structures.

The article is organized as follows: “**Research Methodology**” refers to research methodology followed in this investigation including an accurate description of selected box-beam geometry and materials with several details about the carried out experiments and numerical simulations. “**Correlation Method**” is devoted to the adopted correlation method, while experimental and numerical results are reported and discussed in “**Results and Discussion**”. Main innovative results and outcomes are collected in “**Conclusion**” as a conclusion.

## Research Methodology

A complete dynamic analysis of two coupled box-beam (Table 1) configurations is performed. Two geometrical configurations are selected to demonstrate the structural performance obtained during the design activity.

The first one (Fig. 1) is the same used in Cestino and Frulla [13]. It is composed of two aluminium stiffened panels oriented at 25° designed to achieve a bending-torsion coupling. The stiffeners are symmetric with respect to the

**Table 1** Beam mass and useful length

Beam	Mass [kg]	Length [mm]
Aluminium	2.810	1100
Carbon FRP	1.510	1450

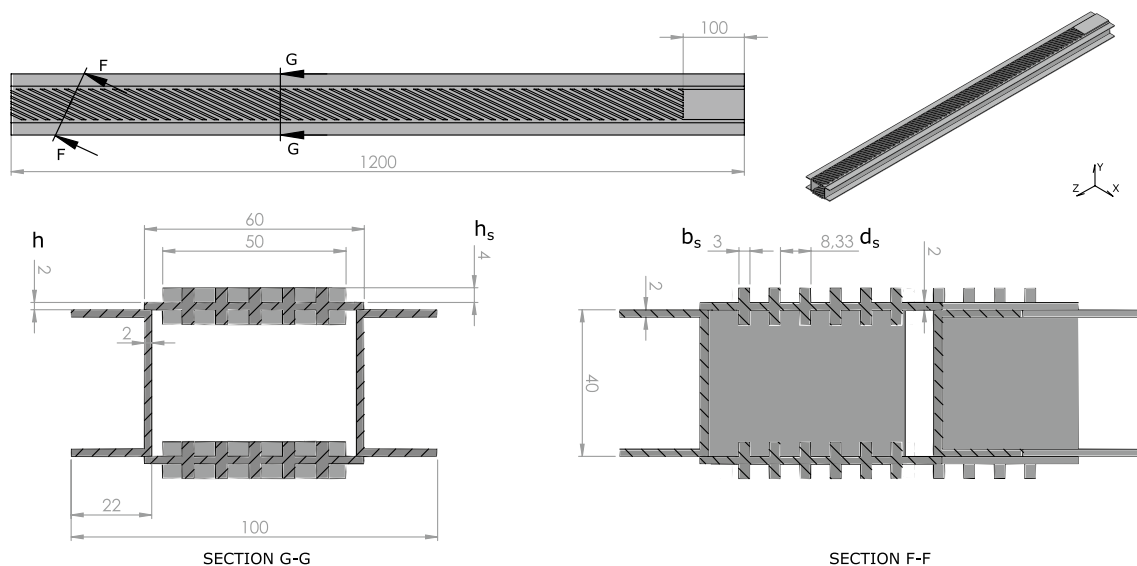


**Fig. 1** Aluminium Beam - Geometry and dimension in mm

**Table 2** Al6060 mechanical and physical properties

Property	Value
Young's modulus, $E$ [MPa]	58,000
Shear Modulus, $G$ [MPa]	21,805
Poisson's ratio, $\nu$	0.33
Mass density, $\rho$ [kg/dm <sup>3</sup> ]	2.66

mid-plane of the skin panel,  $b_s = 3$  mm, the number of stiffeners is  $N_s = 6$  and  $d_s = b/N_s = 8.33$ . The upper and lower plates were obtained by machining a 60 mm wide, 1200 mm long and 10 mm thick aluminium plate (Table 2). According to the EQM procedure, an equivalent-stiffener layer thickness  $h_s = 4$  mm and a plate-wall thickness of the stiffened plate  $h = 2$  mm have been determined. Two C-shaped spars with a constant section 20 mm high, 40 mm wide and with thickness equal to 2 mm, made of the same 6060 aluminium alloy were bonded onto the two stiffened plates. The total beam length of 1200 mm have to be reduced by 100 mm for fixing equipment so the useful length was 1100 mm.

The second beam (Fig. 2) presents a similar configuration already considered by Cestino et al. [17] for static analyses, based on carbon fiber reinforced polymer (CFRP) with unidirectional (UD) T700 carbon/epoxy prepreg with fibers oriented at 18° ([18/18/18/18]), for the upper and lower plates 1 mm thick. The design criterium was the same as the previous configuration related to obtain a bending-torsion coupling effect. Cure conditions 2 h at 135 °C. The vertical web was manufactured by standard C-shaped components of 6060 aluminium alloy ( $E=58,000$  MPa,  $\nu=0.33$ ) with section 20 mm high, 40 mm wide and thickness equal to 2 mm. Mechanical properties adopted for carbon/epoxy prepreg are reported in Table 3. The beam is 1450 mm long and fixture

**Table 3** UD T700/Epoxy mechanical and physical properties

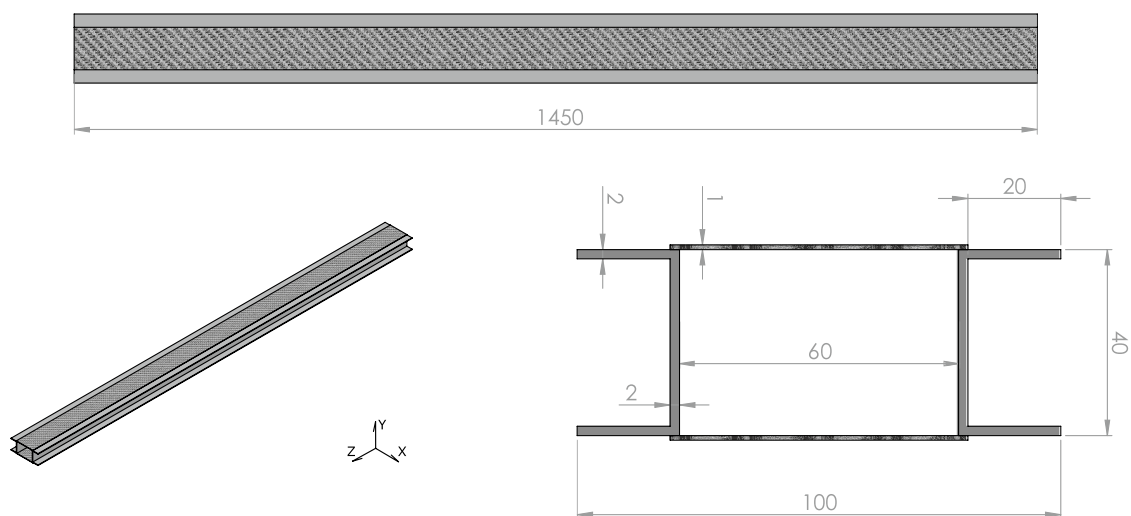
Property	Value
Longitudinal Young's Modulus, $E_1$ [MPa]	118,000
Transverse Young's Modulus, $E_2$ [MPa]	9938
Shear Modulus, $G_{12}$ [MPa]	3400
Poisson's ratio, $\nu$	0.33
Mass Density, $\rho$ [kg/dm <sup>3</sup> ]	1.60

arrangements does not modify this dimension due to specific metal bolted components inside the box.

## Experimental Setup

The aluminium beam and the CFRP beam modal behaviour have been investigated with two experimental activities with similar setup and equipment. The experimental modal tests have been performed using an electrodynamic shaker K200xE01 and a Polytec PSV-500 scanning laser head with proper control box [18] as presented in Fig. 3. LDV is a powerful equipment that provides a contact-less measurement of structural vibration, avoiding mass loading and installation problems of accelerometers. The selected shaker provides large bandwidth of excitation and high frequency resolution, that are useful to conduct modal tests on various types of structures.

The excitation of the mechanical system is obtained through a periodic chirp signal, which consist in a continuous sweep in a defined frequency range. A list of the main experimental parameters adopted during the acquisition with LDV equipment can be found in Table 4. The frequency range was set to 0–1 kHz for both the experimental

**Fig. 2** UD Carbon FRP beam—geometry and dimension in mm

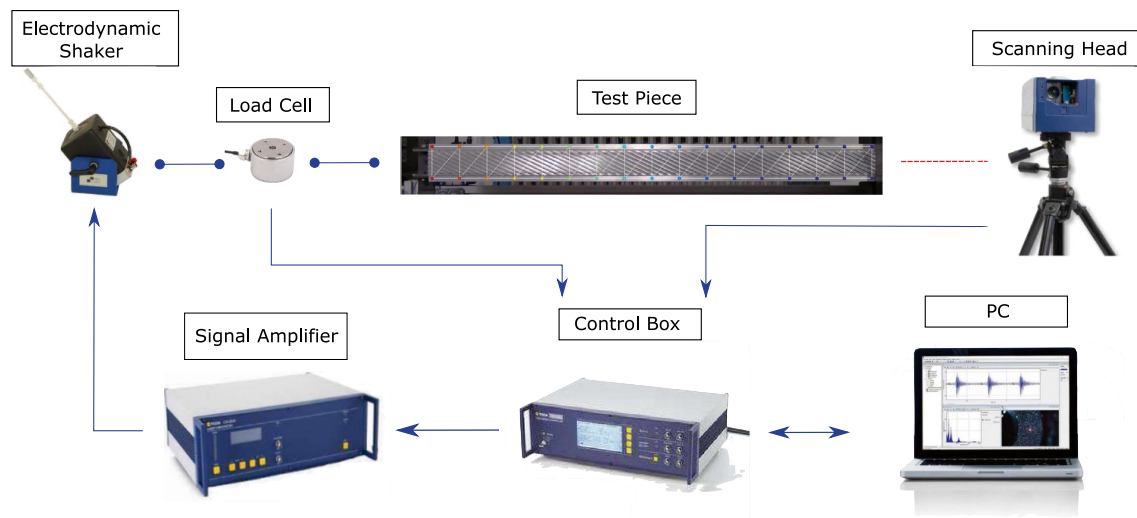


**Fig. 3** Chain of Measurement

activities. This range contains all the modal behaviours relevant for this activity according to the numerical simulations. Despite the excitation signal being periodic and controlled in amplitude a relatively low number of complex averages was considered to be enough for the analysis.

The acquisition time was selected to match exactly the sweep duration of the chirp signal. The distance between the test pieces and the scanning laser head was set equals to 0.8 m. The LDV was positioned in the mid-span of each beam to reduce the angle of divergence of the laser from the main source and thus reduce the misalignment error. The relative sensibility of the LDV for the two experimental activities is provided in Table 4, established after a calibration phase related to material response and structural dimension of the different samples. The experimental setup for LDV tests is shown in Fig. 3.

The box-beam has been considered fixed at one end and free in the other end for both cases in parallel direction with respect to the supporting horizontal test table as shown in Fig. 4. Heavy and stiff steel blocks connected by threaded

rods guarantee the right clamping pressure at the fixed end of the tested beam avoiding structural transversal sliding. The shaker positions along span-wise direction are reported in Table 5 in opposition to LDV. Two different experimental sessions are prepared for each single box-beam: TEST1 and TEST2. The shaker was fixed to an independent aluminum rigid frame which was positioned behind the beams structure.

A typical chain of measurement is summarized here: the control box generates the input signal managed by the PSV Software. The signal is amplified and sent to the electrodynamic shaker selected. An impedance head is installed on the shaker head, it provides acceleration and force signal to the front-end of LDV. The sensor is attached to the beam surface with cyanoacrylate glue. Test samples vibrations are measured and stored from the scanning laser head in every scanning point selected before the acquisition. Single scanning points represent the specific geometric location in which the LDV records all the experimental values necessary to reconstruct the dynamic behavior of the tested structure. Both input and output signals are measured in the time domain. After a single cycle and for every scanning point the front-end system computes the resulting frequency response function (FRF) and send it to the PC for visualization and

**Table 4** Experimental parameters used for modal testing

Property	Aluminium Beam	Carbon UD FRP Beam
Resolution points	36	34
Frequency span [kHz]	0–2	0–2
Window span [kHz]	0–1	0–1
Spectral lines	6400	6400
Averaging Complex	8	8
Shaker amplitude [V]	0.025	0.1
Vibrometer sensibility [mm/s]	50	100

**Table 5** Shaker position from clamped end

Beam	TEST1: Position [mm]	TEST2: Position [mm]
Aluminium	1120	700
Carbon FRP	1450	960

storing. Around 35 measurement points, equally spaced on the upper and lower smooth surface of the test pieces, have been considered in LDV acquisition. PSV software allows a visualization of the mean dynamic behavior of the sample or specific scanning point response.

## Numerical Analysis

Three FEM models have been defined for the numerical simulation: a solid FE model and a shell FE model with equivalent properties for the aluminium case and a shell FE model for the CFRP case. A solid FE model has been considered for the aluminium stiffened beam. Standard TETRA elements with four vertex nodes and material properties according to Table 2 have been considered. The same aluminium stiffened beam has been also simulated using an equivalent material for the stiffened plates. Specific properties as reported in Table 6, have been introduced in a shell FE model by means of equivalent MAT8 material and PCOMP NASTRAN card. Finally, a composite shell FE model was adopted to describe the numerical modal behavior of CFRP beam. The results obtained from the NASTRAN FE modal analysis are reported in Tables 8–9. The nodes which belong to the clamped region of the beam have all translation displacement fixed ( $U_x = U_y = U_z = 0$ ). The Frequency Response Function (FRF) for each case has been computed and compared to the experimental ones as reported in Fig. 5. The glued connections have been considered as perfect bonding and the measured thickness equals to 0.2 mm has been considered negligible. However, some imperfections are possible and can affect the physical test causing minor discrepancies between experimental and numerical results.

Damping was neglected in the initial modal analysis and then estimated experimentally with the Half-Power Bandwidth Method. The damping ratio estimated for the first bending mode and the first torsional mode are reported in Table 7. The simulation were repeated considering the damping ratio and resulting in differences lower than 0.07%

**Table 6** Equivalent single layer material properties

Property	Value
Longitudinal Young's modulus, $E_1$ [MPa]	20888.36
Transverse Young's modulus, $E_2$ [MPa]	0
Shear modulus, $G_{12}$ [MPa]	1636.03
Poisson's ratio, $\nu$	0
Mass density, $\rho$ [ $kg/dm^3$ ]	0.99

**Table 7** Damping ratio

Mode	Value
Aluminium Beam bending mode	0.009
Aluminium Beam torsional mode	0.007
CFRP Beam bending mode	0.016
CFRP Beam torsional mode	0.007

with respect to the natural frequencies of the undamped system. According to the scope of the present work, damping has been neglected in the presentation of the results.

The calculation of the specific equivalent material properties follows the methodology defined by Nemeth [19] and Cestino [13] which results in the following expressions:

$$\begin{aligned} E_{11} &= \left( \frac{E_s b_s}{d_s} \right)_{el-12} ; E_{22} = 0 ; \nu_{12} = 0 ; \\ G_{12} &= \frac{\tau_y^s}{4} \left( \frac{E_s b_s}{d_s} \right)_{el-12} ; G_{13} = \tau_z^s \left( \frac{E_s b_s}{d_s} \right)_{el-12} ; G_{23} = 0 \end{aligned} \quad (1)$$

The equivalent density is obtained imposing the mass of the full equivalent layer equal to the mass of the stiffeners. The thickness of the equivalent layer ( $h_e$ ) is considered equals to the stiffeners height ( $h_s$ ). The thickness can be computed also imposing the equivalence of area, first moment of inertia, second moment of inertia or torsional rigidity depending on which behaviour is dominant. The density should

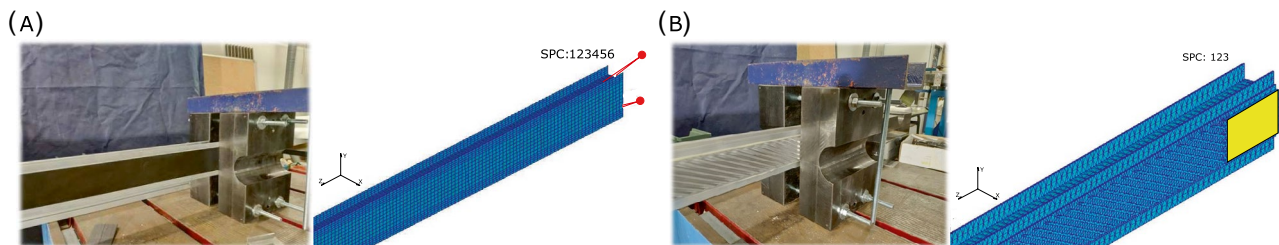


**Fig. 4** Experimental and numerical boundary conditions

**Fig. 5** FRF curve comparison:  
**a** Aluminium Beam; **b** UD  
 Carbon FRP Beam

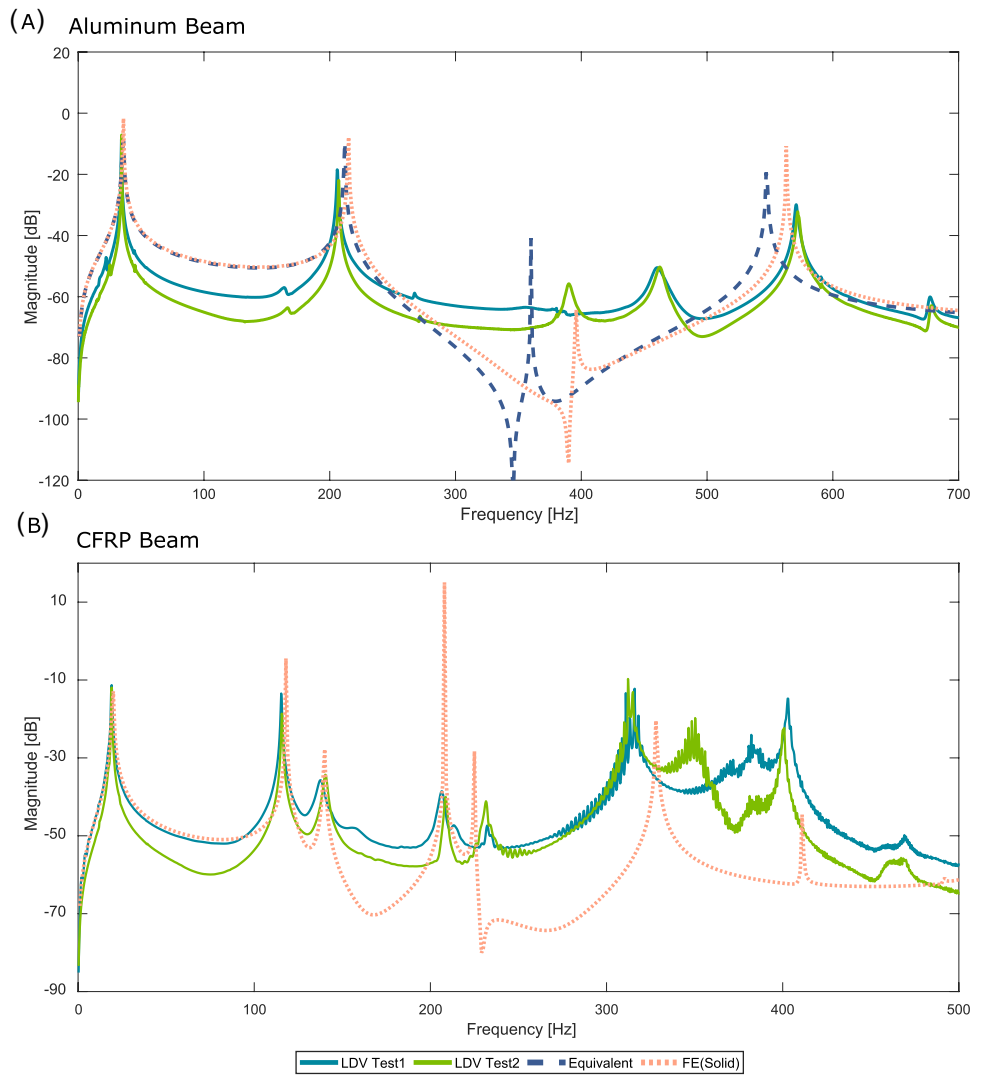


**Table 8** Natural frequencies [Hz] for the aluminium beam compared to numerical and EQM procedure

Aluminium Beam					
Mode	Experimental [Hz]	Num. SOLID [Hz]	Relative diff. [%]	Num. (EQM) [Hz]	Relative diff. [%]
1	34.53	35.82	3.67 (3.74)	35.59	3.02 (3.07)
2	206.90	214.80	3.75 (3.82)	211.77	2.33 (2.35)
3	390.25	395.44	1.32 (1.33)	360.62	7.89 (7.59)
4	571.10	563.14	1.40 (1.39)	547.54	4.21 (4.12)

Relative difference with experimental frequency as reference value within parentheses

be modified accordingly. For the purpose of this work, it is preferred to not discern a priori which among membrane, bending or shear behaviour is dominant. Imposing  $h_e = h_s$  all the aforementioned structural behaviours are consistently represented and this method result more suitable for implementation on commercial Finite Element codes. The

resulting properties for the equivalent single layer material obtained using the configuration of the aluminium beam object of this paper, are listed in Table 6.

More details on the derivation of equivalent single layer model are provided in Appendix A.





## Correlation Method

Modal testing is widely applied to provide a comparison between a predicted dynamic behavior of a structure and what can be observed in a practical situation. Sometimes this process is referred to as ‘validating’ a theoretical model, although to do this effectively, several steps must be taken. The first step consists in a direct and objective comparison of measured and predicted specific dynamic properties. The second step quantifies the extent of differences between the two sets of data. The last steps consist in the identification of the reasons for any discrepancies between measured and predicted behavior and make adjustments or modifications to align the results. At the end of this procedure theoretical or numerical model can be considered as validated for further analysis. Experimental and numerical natural frequencies and mode shapes have been compared. Natural frequencies follow a simple application of equation Eq. 2 determining a relative differences, while Modal Assurance Criterion (MAC) has been applied for mode shapes evaluation. Moreover, experimental and numerical tests have been also evaluated through FRFs comparison with the direct overlap of the different spectral plots. MAC is a statistical indicator used to quantifying the accuracy and the similarity between assumed and determined mode shapes ranging from zero (no similarity) to one (complete similarity) [20]. Equation 3 describes the normalized dot product of two complex modal vectors at each common node (Experimental-Numeric). In particular,  $\Phi_i$  and  $\Phi_j$  are the  $i$ -th and  $j$ -th mode eigenvectors, respectively, the subscript num and exp denotes the eigenvectors origin.

$$\text{Rel. Diff. \%} = \frac{|\omega_{\text{num}} - \omega_{\text{exp}}|}{\left(\frac{\omega_{\text{num}} + \omega_{\text{exp}}}{2}\right)} \cdot 100, \quad (2)$$

$$\text{MAC}_{ij} = \frac{|\Phi_{\text{num}}^{iT} \Phi_{\text{exp}}^j|^2}{(\Phi_{\text{num}}^{iT} \Phi_{\text{num}}^j)(\Phi_{\text{exp}}^{iT} \Phi_{\text{exp}}^j)}. \quad (3)$$

## Results and Discussion

The numerical results, determined according to “[Research Methodology](#)”, and experimental ones have been compared following the procedure reported in this section. Experimental FRFs are shown in Fig. 5, while Tables 8–9 summarize the experimental, FE-solid and FE-EQM natural frequencies with their relative differences. The Auto-MAC and MAC matrices obtained through the application of Eq. 3 for mode-shape comparison are reported in Figs. 6 and 8. Normalized graphical representation of selected eigenvectors from different tests is reported in Figs. 7 and 9, the fringe color describes the relative shape of the transverse displacement (y-displacement) of the beam. This representation directly improves the comparison and evaluation of natural mode shapes with a particular focus on the bending-torsion coupled modes for selected resonance frequencies.

### TEST1: Aluminium Beam- Tip Excitation

The first test conducted on the aluminum beam with tip excitation has revealed three global vibration modes under 600 Hz as expected by numerical simulation. Figure 5a reports the comparison of natural frequencies and, on the other hand, Fig. 7 shows the mode shapes differences.

However, two mayor discrepancies have been identified with respect to the FEM models: the experimental FRF curve (Fig. 5a) presents four peaks, which is apparently in contrast with the numerical results. Graphical representation of the mode found between 400 and 500 Hz revealed a modal shape comparable to the characteristic following mode at 570 Hz but inconsistent with the boundary conditions applied. The presence of this mode shape could be linked to the reduced number of scanning points selected for the beam. A relatively low number of scanning points can lead to lower accuracy and can result in the presence of anomalies. On the other hand, a high number of scanning points increase dramatically the acquisition time. For this reason, the number of scanning point has been

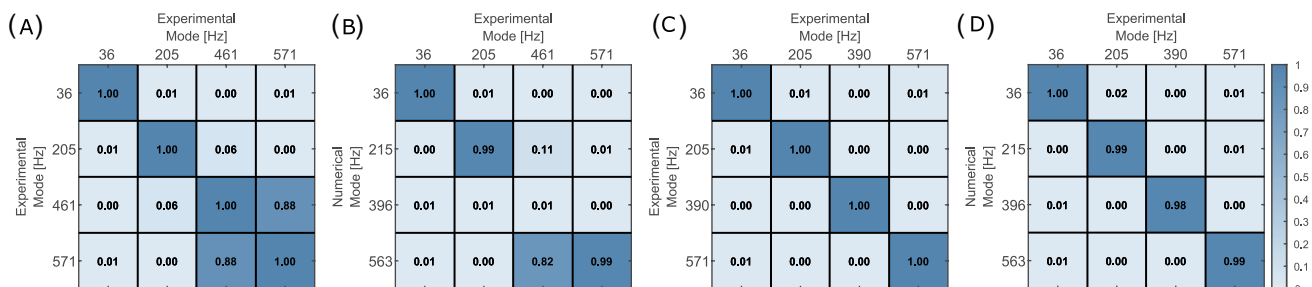


**Fig. 6** MAC matrices for the comparison of mode shapes for aluminium beam. **A** Auto-MAC of TEST1 experimental modes, **B** MAC of TEST1 experimental and numerical modes, **C** Auto-MAC of TEST2 experimental modes, **D** MAC of TEST2 experimental and numerical modes



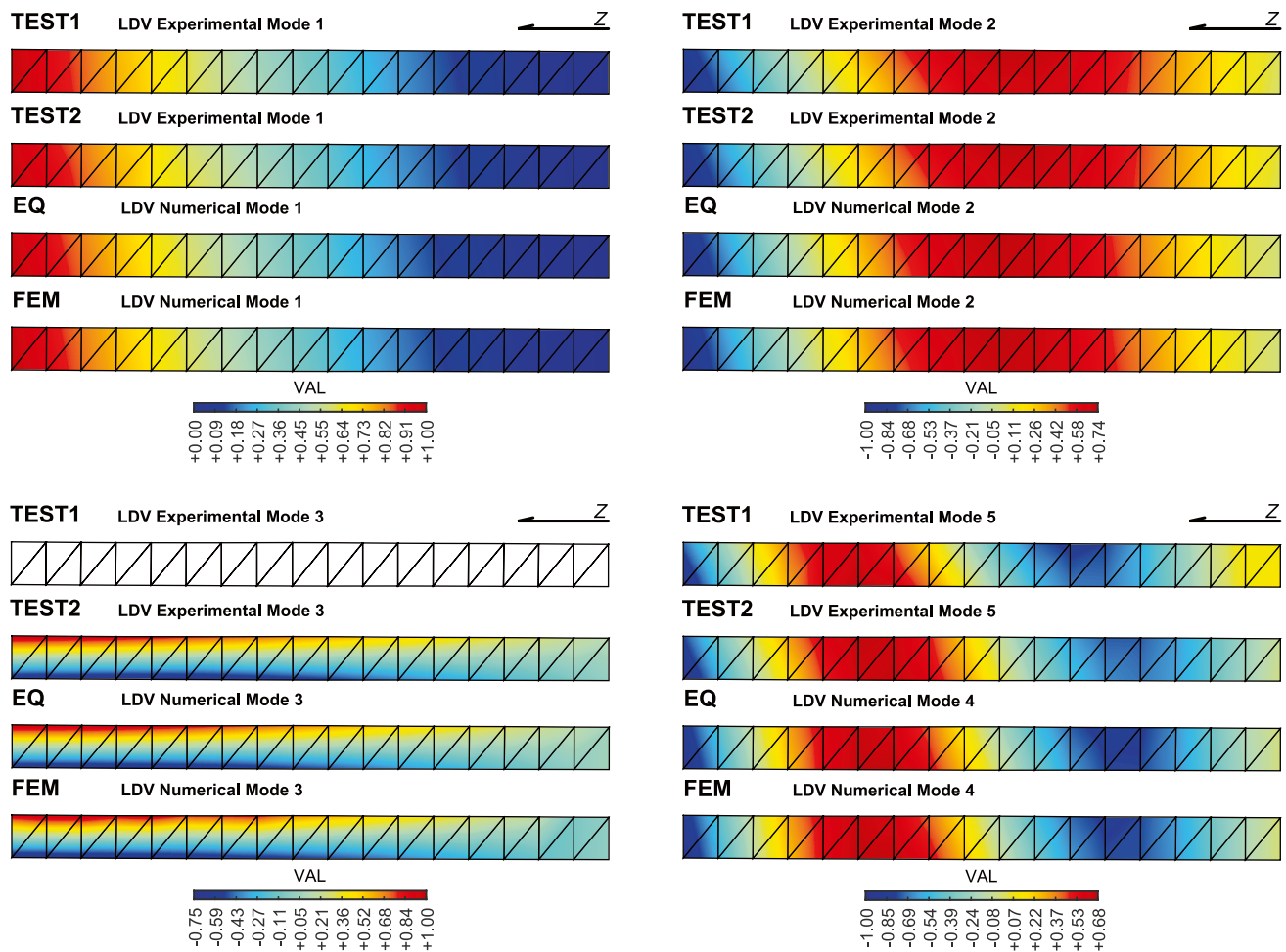


**Fig. 7** Natural Mode Shape Comparison of the first modes of the aluminium beam: Every mode is compared with relative experimental, numerical and equivalent model results

**Table 9** Natural frequencies [Hz] for an UD Carbon FRP beam compared to numerical procedure

Mode	UD Carbon FRP Beam		
	Experimental [Hz]	Numerical [Hz]	Relative diff. [%]
1	19.06	19.65	3.05 (3.10)
2	115.30	118.05	2.37 (2.39)
3	140.15	139.71	0.31 (0.31)
4	207.50	208.00	0.24 (0.24)

Relative difference with experimental frequency as reference value within parentheses

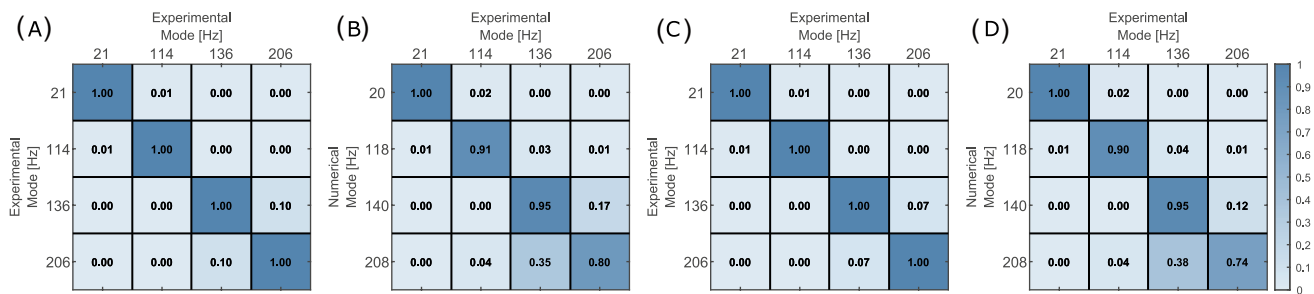
determined as a compromise. Another cause for the difference between numerical and experimental results can be the position of the scanning points, they must be on a flat and reflective surface and they were positioned on a portion of the C-shaped spars on both beams. This can cause the detection of local modes of the spars, these modes can

interfere with the global modes. The analysis of couplings between the global modes and the local modes was not in the scope of this work and for this reason, these combinations were not investigated.

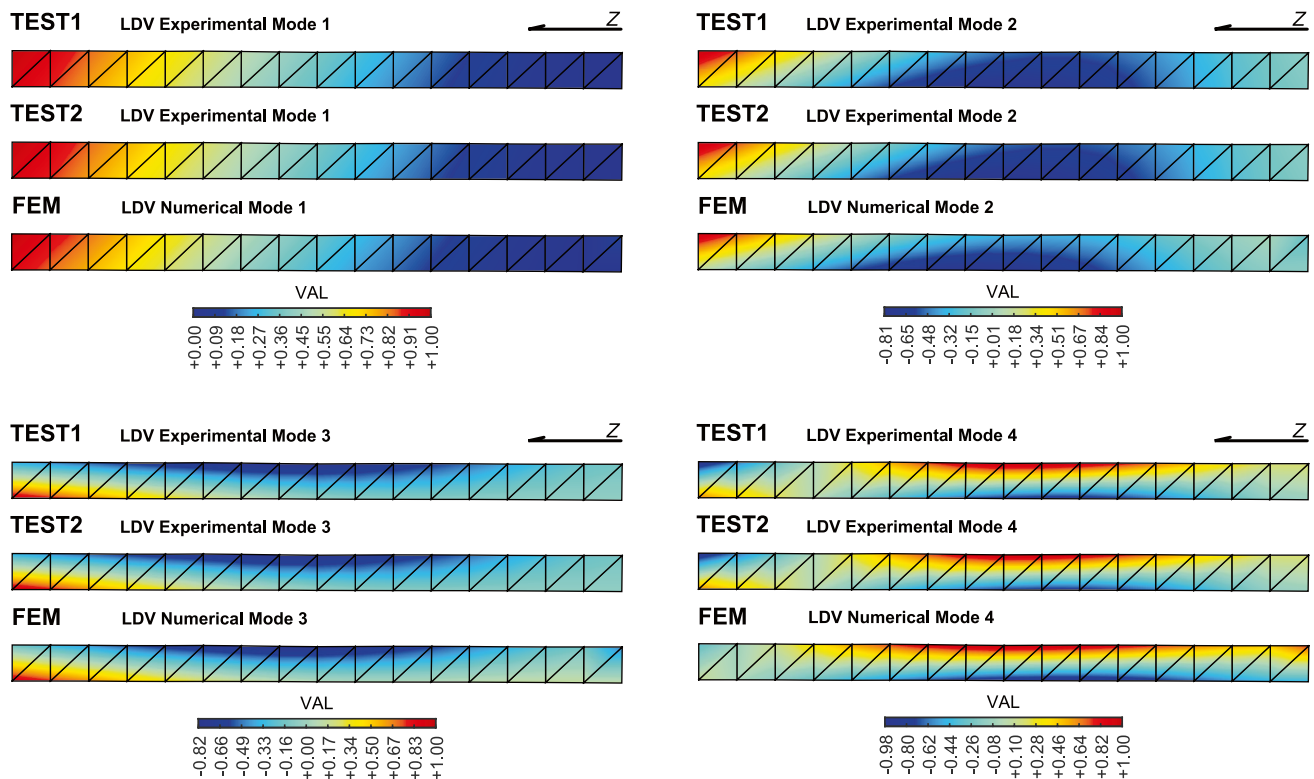
Another difference is related to torsional mode determined around 400 Hz according to FEM simulation. In this case an ex-post evaluation indicated that the excitation at the tip did not produce any torsional mode in the selected bandwidth. The symmetry of the loading through the width (y-axis) of the beam seems responsible for the minor excitation of this third global mode.

Figure 6A and B shows Auto-MAC and MAC matrices related to experimental (TEST1) and numerical comparison. As stated before, the torsional mode is missing as confirmed by the presence of the third mirrored mode according to off-diagonal terms ([3,4]; [4,3]) near to 1.0 for the third and fourth mode. Moreover, the comparison of experimental modes and numerical results for TEST1 confirm that the third bending mode of the aluminium beam does not exist





**Fig. 8** MAC matrices for the comparison of mode shapes for UD carbon FRP beam. **A** Auto-MAC of TEST1 experimental modes, **B** MAC of TEST1 experimental and numerical modes, **C** Auto-MAC of TEST2 experimental modes, **D** MAC of TEST2 experimental and numerical modes



**Fig. 9** Natural Mode Shape Comparison of the first modes of the UD carbon FRP beam: Every mode is compared with relative experimental and numerical results

in the numerical model due to the presence of a zero term on the principal diagonal.

### TEST2: Aluminium Beam-Second Exciting Position

The second test for the aluminium beam was conducted with the shaker positioned at 700 mm from the clamped edge. In this case, all the four modes predicted by the numerical analysis were successfully captured. Observing Fig. 5a, the anomaly already discussed between 400 and 500 Hz is still present.

However, it is possible to notice that the peaks of the experimental FRF curve (green line) are almost coincident with the peaks obtained with the FE model (orange dotted line). As reported in Table 8, the relative errors between experimental and numerical modal frequency are less than 4%. The eigenvectors extracted during this test outlined the same mode shapes as predicted with the FE model and confirmed by graphical representation in Fig. 7. The first, second and fourth are substantially bending modes with a distinguishable torsional participation. Instead, the third mode is torsion mode slightly coupled with the bending one. It is interesting to notice a series of oblique fringes displayed by

the LDV experimental data that have the same inclination of the aluminum sub-stiffeners. A bending torsion coupling effect is thus confirmed highlighting the bending-torsion coupling caused by the oriented aluminum stiffeners.

The EQM numerical model was able to predict the characteristic frequency with a relative error lower than 5% for most of the modes. The torsional mode frequency was slightly underestimated and presents a relative error equal to 7.89%. This could be linked to the EQM approximations transforming a local effect in a distributed one. In particular, the local effects linked to the stiffeners result uniformly distributed on the entire panels decreasing the effect of the bending-torsion coupling in the EQM model.

The modal shapes obtained with the EQM model agree with both the experimental and the numerical ones and presents the same coupling effects. Figure 6C and D show Auto-MAC and MAC for experimental and numerical results pointing out an improvement in correlation with respect to the previous exciting point.

### TEST1: Carbon UD FRP Beam- Tip Excitation

Similar comparison have been performed here for the CFRP box-beam. The experimental FRF curves are reported in Fig. 5b. A satisfactory experimental/numerical correlation has been demonstrated for the first four modes. Assuming the experimental results as the correct representation, minor reported differences should be assigned to the lack in glued connection modelling. The idealized representation adopted in the numerical model brings over stiffness which causes higher frequencies for the subsequent natural modes. After 300 Hz, the experimental FRF curve presents some noise with multiple peaks. This can be related to the local vibration modes of the carbon fiber panels and to the experimental parameters selected and reported in Table 5 for the modal evaluation of the global behaviour of FRF carbon beam. However, the measured natural frequencies present a relative error lower than 4% in comparison with those obtained by means of FE model (Table 9). The graphical visualization of the mode shapes as reported in Fig. 9, shows a good experimental/numerical correlation high degree of coupling are evident for the FRP beam with oblique layup stratification.

Auto-MAC, in Fig. 8a, confirms the consistent behaviour of the modes, while the MAC matrices in Fig. 8b maps the correlation between the experimental vectors and the numerical ones. The increasing value of the off-diagonal terms ([4,3]; [3,4]) is strictly connected to the number of scanning points selected in experimental tests and to the high frequency local modes of composite panels. However, is interesting to note that the fourth experimental natural

mode shapes displayed in Fig. 9, present a relative deformation at the tip of the beam that is consistent with the numerical observation. Some other observations related to slight discrepancies observed in this analysis can be justified by the following items: (a) clamped boundary condition modeled with SPC in the finite element method is a simplification of the ones used during the experimental activity; (b) FE analysis does not consider possible non-linear behaviors of the different structural components; (c) Glue, friction and contacts are not modeled; (d) no damping has been added in the model.

### TEST2: Carbon UD FRP Beam-Second Exciting Point

Table 9 collects experimental and numerical results related to TEST2 CFRP beam. The experimental FRF (Fig. 5) confirms the previously obtained findings. Again, UD Carbon FRP beam response is characterized with high number of local modes that introduces signal noise: increasing experimental resolution is necessary and higher number of measuring points should be introduced. Mode shapes shown in Fig. 9 are very similar to the ones produced during TEST1, the same occurs also for MAC matrices. For this reason, the considerations, and conclusions on TEST1 results can be applied also on TEST2.

## Conclusion

Experimental and numerical vibration response of typical coupled box-beams for aero-structural application have been analyzed and investigated. Validation of previously obtained static results has been provided completing the analysis with dynamical counterpart. The preliminary analytical derivation has been also confirmed and proved for design activity simplification. Aluminium 6060 and UD T700/Epoxy beams with similar coupled performances have been investigated. The aluminum stiffened plates with the metallic box-beam were manufactured by CNC machining, while CFRP panels were produced with the required cure-cycle. Experimental modal analysis has been carried out with typical testing equipment based on a laser Doppler vibrometer (LDV) and a modal electrodynamic shaker K200xE01. Experimental and numerical results have been compared in terms of natural frequencies, graphical mode shapes and modal assurance criterion (MAC) matrices. The obtained relative errors remain below 4% for all situations. MAC diagonal values are ranging from 0.8 to 1, with minor and justifiable exceptions. EQM theory reproduces the modal behavior of metallic case with relative error lower than 8% (either bending and



torsional cases) confirming the validity of the procedure for preliminary design activity. Carbon UD FRP beam analysis confirms the idea of optimizing proper laminate lay-up for specific bending-torsion coupling effects. The adopted design solutions demonstrate that it is possible to achieve the desired dynamic coupling either with oriented fibers or metallic stiffeners. This particular behavior could find an extensive application in wing boxes definition, where such a coupling effect can be used to prevent aeroelastic instability. Finally, the good agreement with experimental test and EQM results confirms this methodology as a valuable instruments for the early design stages of metal wing-box dramatically reducing the real structure complexity and computational costs with satisfactory accuracy.

## Appendix A EQM derivation

According to Nemeth [19] and [13], the strains of the repeating-element stiffeners are considered equal to the corresponding plate strains imposing a kinematic equivalence. Furthermore, the plate stresses resultants are related to the beam forces and moments. From hereafter the kinematic and static equivalence is referred to as direct compatibility. Following Nemeth assumptions, the variation of the stress resultants across the width of the stiffeners are neglected. The direct compatibility is derived for a family of rectilinear stiffeners equally spaced, with  $d_s$  being the stiffeners spacing and oriented with an angle  $\Psi_s$  with respect to the x-axis of the plate. Prismatic rectangular stiffeners are considered for this derivation, it is assumed that stiffeners are in the symmetric configuration and perfectly bonded to the skin. The points of the beam refer to a local Cartesian coordinates system (1,2,3), oriented as the stiffeners. Direct compatibility is obtained with the presumption that the strains of the stiffeners are identical to the strains of the corresponding point of the equivalent layer neglecting the variation across the width. In addition, the bending of the stiffener in the plane parallel to the plate mid-plane is considered negligible and, for this reason, the variation of strains across the width of the equivalent-stiffener layer can be neglected. Furthermore, it is presumed that the eccentric stiffener contributes only half of the in-plane shearing strain and half of the change in the surface twist of the equivalent-stiffener layer. To establish the static equivalence between the repetitive stiffened-panel and the equivalent plate elements, the stress resultants of the equivalent plate have to be equal to the beam forces and moments of the beam following Timoshenkos hypothesis

for the straight beam. After some algebraic manipulation the stress resultants of the stiffeners layer can be written as:

$$\begin{aligned} N_x^{\text{stiff}} &= \frac{E_s A_s}{d_s} (\epsilon_{xx}^0 + \bar{z} k_{xx}) & N_{xy}^{\text{stiff}} &= \frac{k_y G_s A_s}{d_s} (\gamma_{xy}^0 + \bar{z} k_{xy}) \\ M_x^{\text{stiff}} &= \frac{E_s A_s \bar{z}}{d_s} (\epsilon_{xx}^0 + \frac{E_s I_{yy}}{d_s} \bar{z} k_{xx}) & M_{xy}^{\text{stiff}} &= \frac{k_y G_s A_s \bar{z}}{2 d_s} \gamma_{xy}^0 + \frac{G_s I_t}{2 d_s} k_{xy} \\ Q_{xz}^{\text{stiff}} &= \frac{k_z G_s A_s}{d_s} \gamma_{xy}^0 \end{aligned} \quad (A1)$$

The constitutive equations for the stiffeners in terms of the strain expressed in the equivalent plate can be written as follows:

$$\begin{aligned} \begin{Bmatrix} N_x \\ [0.5em] N_y \\ [0.5em] N_{xy} \end{Bmatrix} &= \begin{bmatrix} \frac{E_s A_s}{d_s} & 0 & 0 \\ 0 & 0 & 0 \\ 0 & 0 & \frac{k_y G_s A_s \bar{z}}{4 d_s} \end{bmatrix} \begin{Bmatrix} \epsilon_{xx}^0 \\ [0.5em] \epsilon_{yy}^0 \\ [0.5em] \gamma_{xy}^0 \end{Bmatrix} \\ &+ \begin{bmatrix} \frac{E_s A_s \bar{z}}{d_s} & 0 & 0 \\ 0 & 0 & 0 \\ 0 & 0 & \frac{k_y G_s A_s \bar{z}}{4 d_s} \end{bmatrix} \begin{Bmatrix} k_{xx}^0 \\ [0.5em] k_{yy}^0 \\ [0.5em] k_{xy}^0 \end{Bmatrix} \end{aligned} \quad (A2)$$

$$\begin{aligned} \begin{Bmatrix} M_x \\ [0.5em] M_y \\ [0.5em] M_{xy} \end{Bmatrix} &= \begin{bmatrix} \frac{E_s A_s \bar{z}}{d_s} & 0 & 0 \\ 0 & 0 & 0 \\ 0 & 0 & \frac{k_y G_s A_s \bar{z}}{4 d_s} \end{bmatrix} \begin{Bmatrix} \epsilon_{xx}^0 \\ [0.5em] \epsilon_{yy}^0 \\ [0.5em] \gamma_{xy}^0 \end{Bmatrix} \\ &+ \begin{bmatrix} \frac{E_s I_s}{d_s} & 0 & 0 \\ 0 & 0 & 0 \\ 0 & 0 & \frac{G_s I_t}{24} \end{bmatrix} \begin{Bmatrix} k_{xx}^0 \\ [0.5em] k_{yy}^0 \\ [0.5em] k_{xy}^0 \end{Bmatrix} \end{aligned} \quad (A3)$$

$$\begin{aligned} \begin{Bmatrix} Q_{xy} \\ [0.5em] Q_{xz} \end{Bmatrix} &= \begin{bmatrix} 0 & 0 \\ 0 & \frac{k_y G_s A_s}{2 d_s} \end{bmatrix} \begin{Bmatrix} \gamma_{xz} \\ [0.5em] \gamma_{yz} \end{Bmatrix} \end{aligned} \quad (A4)$$

Finally, a rotation must be performed to align the beam reference system to the plate reference system ( $x, y, z$ ), then one can obtain the expression of the stiffness matrices of the usual Reissner-Mindlin plate:



$$\begin{aligned}
\bar{Q}_{11}^{\text{stiff}} &= \frac{E_s b_s}{d_s} \cos^2 \Psi_s \left( \cos^2 \Psi_s + \tau_y^s \sin^2 \Psi_s \right) \\
\bar{Q}_{12}^{\text{stiff}} &= \frac{E_s b_s}{d_s} \cos^2 \Psi_s \sin^2 \Psi_s \left( 1 - \tau_y^s \right) \\
\bar{Q}_{16}^{\text{stiff}} &= \frac{E_s b_s}{d_s} \cos \Psi_s \sin \Psi_s \left( \cos^2 \Psi_s - \frac{\tau_y^s}{2} \cos 2\Psi_s \right) \\
\bar{Q}_{22}^{\text{stiff}} &= \frac{E_s b_s}{d_s} \sin^2 \Psi_s \left( \sin^2 \Psi_s + \tau_y^s \cos^2 \Psi_s \right) \\
\bar{Q}_{26}^{\text{stiff}} &= \frac{E_s b_s}{d_s} \cos \Psi_s \sin \Psi_s \left( \sin^2 \Psi_s + \frac{\tau_y^s}{2} \cos 2\Psi_s \right) \\
\bar{Q}_{66}^{\text{stiff}} &= \frac{E_s b_s}{d_s} \left( \cos^2 \Psi_s \sin^2 \Psi_s + \frac{\tau_y^s}{4} \cos^2 \Psi_s \right) \\
\bar{Q}_{44}^{\text{stiff}} &= \frac{E_s b_s \tau_z^{\text{stiff}}}{d_s} \sin^2 \Psi_s \\
\bar{Q}_{45}^{\text{stiff}} &= \frac{E_s b_s \tau_z^{\text{stiff}}}{d_s} \sin \Psi_s \cos \Psi_s \\
\bar{Q}_{55}^{\text{stiff}} &= \frac{E_s b_s \tau_z^{\text{stiff}}}{d_s} \cos^2 \Psi_s
\end{aligned} \quad (\text{A5})$$

where  $\tau_y^s = \frac{k_y^2 G_s}{E_s}$ ,  $\tau_z^s = \frac{k_z^2 G_s}{E_s}$  are the in-plane and transverse shear-deformation parameters,  $k_y^2$  and  $k_z^2$  are the respective correction factor,  $E_s$  is the Young's Modulus of the stiffener,  $b_s$  and  $d_s$  are the stiffeners width and spacing, respectively. It should be noted that the resulting matrix  $[\bar{Q}]$  for the straight stiffener is singular; particularly, from the equation in (2) is worth noting that, the rank is 2. If one aim to derive the equivalent properties of the UD material, one has:

$$\begin{aligned}
E_{11} &= \left( \frac{E_s b_s}{d_s} \right)_{el-12}; E_{22} = 0; \nu_{12} = 0; \\
G_{12} &= \frac{\tau_y^s}{4} \left( \frac{E_s b_s}{d_s} \right)_{el-12}; G_{13} = \tau_z^s \left( \frac{E_s b_s}{d_s} \right)_{el-12}; G_{23} = 0
\end{aligned} \quad (\text{A6})$$

More details concerning Eqs. (A1)–(A6), can be found in [15] and [19].

**Funding** Open access funding provided by Politecnico di Torino within the CRUI-CARE Agreement.

## Declarations

**Conflict of interest** The authors have no relevant financial or non-financial interests to disclose.

**Open Access** This article is licensed under a Creative Commons Attribution 4.0 International License, which permits use, sharing, adaptation, distribution and reproduction in any medium or format, as long as you give appropriate credit to the original author(s) and the source, provide a link to the Creative Commons licence, and indicate if changes were made. The images or other third party material in this article are included in the article's Creative Commons licence, unless indicated otherwise in a credit line to the material. If material is not included in the article's Creative Commons licence and your intended use is not permitted by statutory regulation or exceeds the permitted use, you will need to obtain permission directly from the copyright holder. To view a copy of this licence, visit <http://creativecommons.org/licenses/by/4.0/>.

**Open Access** This article is licensed under a Creative Commons Attribution 4.0 International License, which permits use, sharing, adaptation, distribution and reproduction in any medium or format, as long as you give appropriate credit to the original author(s) and the source, provide a link to the Creative Commons licence, and indicate if changes were made. The images or other third party material in this article are included in the article's Creative Commons licence, unless indicated otherwise in a credit line to the material. If material is not included in the article's Creative Commons licence and your intended use is not permitted by statutory regulation or exceeds the permitted use, you will need to obtain permission directly from the copyright holder. To view a copy of this licence, visit <http://creativecommons.org/licenses/by/4.0/>.

## References

1. Frulla G (2004) Aeroelastic behaviour of a solar-powered high-altitude long endurance unmanned air vehicle (HALE-UAV) slender wing. *Proc Inst Mech Eng Part G* 06(218):179–188. <https://doi.org/10.1243/0954410041872889>
2. Romeo G, Frulla G, Cestino E, Marzocca P, Tuzcu I (2006) Non-linear aeroelastic modeling and experiments of flexible wings. <https://doi.org/10.2514/6.2006-2186>
3. Romeo G, Frulla G, Cestino E, Marzocca P. Non-linear aeroelastic behavior of highly flexible HALE wings. In *Proceedings of the 25th ICAS Congress, Hamburg, Germany, 3–8 September 2006*; pp 1–11
4. Frulla G, Cestino E, Marzocca P (2010) Critical Behaviour of Slender Wing Configurations. *Proc Inst Mech Eng Part G* 05(224):587–600. <https://doi.org/10.1243/09544100JAERO553>
5. Cestino E, Frulla G, Spina M, Catelani D, Linari M (2019) Numerical simulation and experimental validation of slender wings flutter behaviour. *Proc Inst Mech Eng Part G* 233(16):5913–5928. <https://doi.org/10.1177/0954410019879820>
6. Gürdal Z, Tatting BF, Wu K (2008) Variable stiffness composite panels: effects of stiffness variation on the in-plane and buckling response. *Compos A Appl Sci Manuf* 05(39):911–922. <https://doi.org/10.1016/j.compositesa.2007.11.015>
7. Kapania R, Li J, Kapoor H (2005) Optimal Design of Unitized Panels with Curvilinear Stiffeners. <https://doi.org/10.2514/6.2005-7482>
8. Benscoter SU, MacNeal RH (1952) Equivalent plate theory for a straight multicell wing. *NACA TN. Hanover, MD, USA, September 1952*; (2786). <https://doi.org/10.1243/0954410041872889>
9. Jaunky N, Knight N, Ambur D (1996) Formulation of an improved smeared stiffener theory for buckling analysis of grid-stiffened composite panels. *Compos B Eng* 12(27):519–526. [https://doi.org/10.1016/1359-8368\(96\)00032-7](https://doi.org/10.1016/1359-8368(96)00032-7)
10. Jutte CV, Stanford BK (2014) Aeroelastic tailoring of transport aircraft wings: state-of-the-art and potential enabling technologies. *NASA TM. Hanover, MD, USA, 1 April*; (218252)
11. Danzi F, Cestino E, Frulla G, Gibert J (2018) Numerical and experimental validation of unitized box beam model. In *Proceedings of the 31st International Congress of the Aeronautical Sciences (ICAS), Belo Horizonte, Brazil, 9–14 September 2018*
12. Cestino E, Frulla G, Marzocca P (2013) A reduced order model for the aeroelastic analysis of flexible wings. *SAE Int J Aerosp* 07(6):447–458. <https://doi.org/10.4271/2013-01-2158>
13. Cestino E, Frulla G (2014) Analysis of slender thin-walled anisotropic box-beams including local stiffness and coupling effects.



- Aircraft Eng Aerosp Technol 07:86. <https://doi.org/10.1108/AEAT-10-2012-0159>
14. Martins J, Kennedy G, Kenway G (2014) High aspect ratio wing design: optimal aerostructural tradeoffs for the next generation of materials. In: 52nd AIAA Aerospace Sciences Meeting - AIAA Science and Technology Forum and Exposition, SciTech. <https://doi.org/10.2514/6.2014-0596>
15. Danzi F, Cestino E, Frulla G, Gibert J (2017) Equivalent plate model of curvilinear stiffened panels. In: Proceedings of the 7th International Conference on Mechanics and Materials in Design, Albufeira, Portugal, 11–15 June 2017
16. Praticó L, Galos J, Cestino E, Frulla G, Marzocca P (2019) Experimental and numerical vibration analysis of plates with curvilinear sub-stiffeners. Eng Struct 12(209):109956. <https://doi.org/10.1016/j.engstruct.2019.109956>
17. Cestino E, Frulla G, Piana P, Duella R (2020) Numerical/experimental validation of thin-walled composite box beam optimal design. Aerospace 07(7):111. <https://doi.org/10.3390/aerospace7080111>
18. Polytec Vibrometry. April 2019. <https://www.polytec.com/eu>
19. Nemeth M (2011) NASA/TP-20—a treatise on equivalent-plate stiffnesses for stiffened laminated-composite plates and plate-like lattices
20. Ewins D (2000) Modal testing, theory, practice and application, 2nd edn. Research Studies Press LTD., Baldock

**Publisher's Note** Springer Nature remains neutral with regard to jurisdictional claims in published maps and institutional affiliations.